

1 **Evidence of abrupt transitions between sea ice**
2 **dynamical regimes in the East Greenland marginal ice**
3 **zone**

4 **Daniel M. Watkins¹, Angela C. Bliss², Jennifer K. Hutchings³, Monica M.**
5 **Wilhelmus¹**

6 ¹Center for Fluid Mechanics, School of Engineering, Brown University, Providence, RI

7 ²Cryospheric Sciences Laboratory, NASA Goddard Space Flight Center, Greenbelt, MD

8 ³College of Earth, Ocean, and Atmospheric Sciences, Oregon State University, Corvallis, OR

9 **Key Points:**

- 10 • Ice dynamics measured with two new Lagrangian datasets show strong bathymetry
11 dependent differences over short spatial scales
- 12 • Wind variability is insufficient to describe drift variability in regions with abrupt
13 changes in bathymetry and large gradients in currents
- 14 • Drifting buoy observations show a spatially heterogeneous imprint of tidal currents
15 on ice dynamics

Corresponding author: Monica M. Wilhelmus, mmwilhelmus@brown.edu

Abstract

Sea ice modulates the energy exchange between the atmosphere and the ocean through its kinematics. Marginal ice zone (MIZ) dynamics are complex and are not well resolved in routine observations. Here, we investigate sea ice dynamics in the Greenland Sea MIZ using in situ and remote sensing Lagrangian drift datasets. These datasets provide a unique view into ice dynamics spanning spatial scales. We find evidence of tidal currents strongly affecting sub-daily ice motion. Velocity anomalies show abrupt transitions aligned with gradients in seafloor topography, indicating changes in ocean currents. Remote-sensed ice floe trajectories derived from moderate resolution satellite imagery provide a view of small-scale variability across the Greenland continental shelf. Ice floe trajectories reveal a west-east increasing velocity gradient imposed by the East Greenland Current, with maximum velocities aligned along the continental shelf edge. These results highlight the importance of small scale ocean variability for ice dynamics in the MIZ.

Plain Language Summary

Sea ice in the Arctic Ocean plays an important role in climate due to its influence on ocean circulation and air-sea energy exchange. Ice motion results from competing and interacting effects of winds, ocean currents, and internal ice stresses. This study uses two novel observational datasets to analyze ice motion in the Greenland Sea and Fram Strait marginal ice zones. We find abrupt changes in the primary causes of ice motion associated with seafloor topography. In shallow seas, strong tidal currents affect ice drift, resulting in repeated opening and closing of the ice. Near the shelf edge, boundary currents increase ice drift speeds, causing ice pack shear. Sea ice models that ignore small-scale ocean currents will underestimate ice deformation.

1 Introduction

The Arctic is warming at over twice the rate of the global average as a result of rising greenhouse gas concentrations (Taylor et al., 2022). A hallmark of Arctic change is a thinning and retreating ice pack (Maslanik et al., 2007; Comiso et al., 2017). Areas of sea ice decline are seeing stronger momentum transfer to the ocean (Polyakov et al., 2020) and intensifying ocean eddies (Manucharyan et al., 2022), amidst other effects (Feldl et al., 2020). Furthermore, previously ice-bound sea routes have rising ship traffic as the ice edge moves northward (Boylan, 2021; Dawson et al., 2018), increasing the potential need for accurate drift forecasts.

Quantifying sea ice dynamics in the MIZ has been an ongoing challenge (Dumont, 2022). In situ sea ice motion measurements are primarily retrieved from moorings and drifting buoys. These instruments are difficult to deploy and generally exhibit a low residence time in MIZ. As a result, there are rarely multiple buoys in the MIZ at any given time. Observations from numerous drift expeditions have demonstrated a tight coupling between ice and ocean variability in the MIZ at small and moderate length and time scales (Leppäranta & Hibler, 1987), including effects of eddies (Morison et al., 1987), boundary currents (Quadfasel et al., 1987), waves (Squire, 2020), inertial oscillations (Lammert et al., 2009; Gimbert et al., 2012), and tidal currents (Heil et al., 2008; Vasulkar et al., 2022). Remote sensing provides an invaluable complement (e.g. Kozlov et al., 2020; Manucharyan et al., 2022), however low data acquisition rates (on the order of days) inherently limit the physical processes being resolved (Kwok, 2010). Sea ice dynamics at sub-daily time scales, for instance, are important for measuring lead opening rates and ridging (Hutchings et al., 2011), key parameters for modeled sea ice growth and air-ocean fluxes, as well as for resolving tidal and inertial motion. Furthermore, drift estimates from microwave radiometers have higher uncertainty during the summer due to melt processes (Tschudi et al., 2020) and due to increased small-scale variability (Yoshizawa et al., 2023).

65 This study aims to characterize marginal ice dynamics in the Eastern Greenland
66 Coast and the Fram Strait region across a broad range of scales and throughout a full
67 season. The complex bathymetry surrounding the Fram Strait and Svalbard is known
68 to result in strong, spatially heterogenous tidal currents (Padman et al., 1992; Fer et al.,
69 2015; Vasulkar et al., 2022) as well as narrow and fast boundary currents (Foldvik et al.,
70 1988; Richter et al., 2018). The spatial heterogeneity of the region, compounded by high
71 interannual variability (Smedsrud et al., 2017), makes it difficult to inter-compare results
72 from prior drift expeditions. As coupled models begin to achieve sufficient resolution to
73 capture small-scale sea ice-ocean interactions (Arbic, 2022), comprehensive observations
74 are needed to constrain models and evaluate model performance, especially in high lat-
75 itudes where uncertainties in small-scale ocean variability (including tides) result in large
76 inter-model differences (Stammer et al., 2014; Zaron & Elipot, 2021). To this end, we
77 leverage two new observational datasets, each providing Lagrangian measures of ice motion:
78 buoy drift trajectories from the Multidisciplinary drifting Observatory for the Study
79 of Arctic Climate (MOSAiC, Nicolaus et al. (2022)) and ice floe trajectories obtained
80 from moderate resolution remote sensing imagery via the Ice Floe Tracker algorithm (IFT,
81 (Lopez-Acosta et al., 2019)). The MOSAiC drift trajectories represent the highest density
82 of in situ ice dynamics observations yet collected. Ice floe trajectories from IFT allow
83 investigation of variation in ice motion at high resolution, as the motion of individual
84 ice floes is measured rather than the area-averaged velocity that is provided by tradi-
85 tional remote-sensing velocity products, and provide a step towards filling the summer
86 gap in satellite-based drift observations.

87 2 Data and Methods

88 2.1 MOSAiC Drift Trajectories

89 Drift trajectories ($n=108$) from sea ice buoys deployed during the MOSAiC Expe-
90 dition were selected such that trajectories (a) contained at least 30 days of data between
91 May 1st and September 1st 2020, (b) had sampling rates of at least once every two hours,
92 and (c) drifted through the Fram Strait. Buoys were deployed in an array surrounding
93 an instrumented Central Observatory (CO) (Krumpen & Sokolov, 2020; Nicolaus et al.,
94 2022). Distance between buoys in the MOSAiC Distributed Network (DN, red lines in
95 Figure 1) ranged from less than 1 to 60 km from the CO on May 1st. Nine additional
96 buoys in the Extended Distributed Network (ExDN, gold trajectories in Figure 1) were
97 between 150 and 530 km away from the CO. Positions were interpolated to a 1-hour grid
98 using cubic splines following de-spiking. Drift velocity was computed using centered dif-
99 ferences after projecting buoy positions onto the NSIDC North Polar Stereographic grid.
100 Sea ice concentration (SIC) from AMSR2 (Meier et al., 2018) was interpolated to indi-
101 vidual buoy positions to find the last date where the buoy remains in sea ice ($SIC > 0$).
102 Hourly 10-m wind velocity from the ERA5 reanalysis (Hersbach et al., 2020) was inter-
103 polated to buoy and ice floe coordinates. Bathymetry data was obtained from the In-
104 ternational Bathymetric Chart of the Arctic Ocean version 4.1 (Jakobsson et al., 2020).
105 Observations at the DN are summarized via median and percentiles for robustness against
106 outliers and to avoid making assumptions about the shape of the distribution.

107 2.2 Ice Floe Tracker algorithm

108 The Ice Floe Tracker (IFT) algorithm (Lopez-Acosta et al., 2019) was used to iden-
109 tify and track sea ice floes in 250 m resolution optical imagery from the Moderate Res-
110 olution Imaging Spectroradiometer (MODIS) spanning the spring-to-summer transition
111 from 2003 to 2020. IFT is a feature-tracking algorithm and can resolve floes with areas
112 of at least 1 km². Corrected-reflectance MODIS imagery was downloaded from NASA
113 Worldview (<https://worldview.earthdata.nasa.gov>). Daytime MODIS images from
114 both Aqua and Terra satellites were analyzed and assigned timestamps using the Satel-

115 lite Overpass Identification Tool (Hatcher et al., 2022). Both Aqua and Terra provide
 116 daily observations, with time offsets between the two satellite images of between 20 and
 117 90 minutes. Floe trajectories were resampled to daily resolution prior to calculating daily
 118 displacement, with gaps of at most 1 day in length filled by linear interpolation. In to-
 119 tal, drift trajectories (2-22 days) are available from 15,637 floes; median trajectory length
 120 is 2 days, and the total number of estimated drift displacements is 42,696.

121 2.3 Frequency analysis

122 Rotary spectral analysis was performed using the University of Hawaii PyCurrents
 123 Python library (<https://currents.soest.hawaii.edu/hg/pycurrents/>). Velocities
 124 for 20-day trajectory segments were de-trended by removing the centered 35-hour mean,
 125 filtered with a Hann window. Resulting spectra were then smoothed with a 3-point box-
 126 car filter. Note that while changing the size of the de-trending window affects the mag-
 127 nitude of the spectra for lower frequencies, it does not alter the position of spectral peaks.

128 The contributions of diurnal and semi-diurnal tides to the sea ice velocity were de-
 129 termined from harmonic analysis as in Pease et al. (1995). The harmonic model has the
 130 form

$$X'(t) = C + Dt + \sum_{k=1}^6 A_k \cos \omega_k t + B_k \sin \omega_k t + \epsilon(t), \quad (1)$$

131 where $X'(t) = X - \bar{X}$ is the position anomaly in polar stereographic coordinates rela-
 132 tive to the centered 35-hour mean, t is the time, C, D, A_k , and B_k are unknowns, and
 133 ω_k are the frequencies of the O1, K1, N2, M2, and S2 tidal constituents. The model is
 134 solved for each Cartesian position component separately. Maximum tidal currents were
 135 estimated by calculating velocity using centered differences on the predicted position anoma-
 136 lies then calculating the daily maximum of these velocities. Model fit was evaluated with
 137 the coefficient of determination.

138 2.4 Deformation analysis

139 The horizontal deformation of sea ice was computed via the Green's Theorem method
 140 (Hutchings et al., 2012, 2018). Strain rates were estimated using sets of buoy arrays man-
 141 ually identified from buoy positions on the first of the month (00:00 UTC) and filtered
 142 with a 5-km spatial filter. Arrays of three or four buoys were selected to provide full, non-
 143 overlapping coverage of the sea ice while reducing the occurrence of skinny triangles lead-
 144 ing to inaccurate strain rate estimates. As a result, 80, 74, and 70 arrays were produced
 145 for May, June, and July, respectively. Hourly strain rates were computed for each indi-
 146 vidual array during the month in which the array configuration was defined, and a time
 147 series was constructed by appending the mean strain rate components (divergence and
 148 maximum shear) across all arrays for each month. Strain rates were not computed fol-
 149 lowing breakup of the CO on 31 July 2020 (Nicolaus et al., 2022). The mean divergence
 150 rate was computed as an area weighted mean to account for variation in array size across
 151 the DN.

152 3 Overview of MOSAiC summer drift

153 From May to September, 2020, the MOSAiC Distributed Network (DN) transitioned
 154 from central Arctic pack ice, through the Fram Strait, and into the East Greenland Cur-
 155 rent, with most buoys eventually exiting the MIZ into the Greenland Sea (Figure 1, left
 156 panel). We approximate the transition times in the following paragraphs by providing
 157 the dates for buoy 2020P225, which was deployed near the Central Observatory; note
 158 that the DN had an effective radius of ≈ 60 km, so crossing an underwater feature such
 159 as a shelf edge at a constant speed of 0.2 m/s takes nearly 7 days.

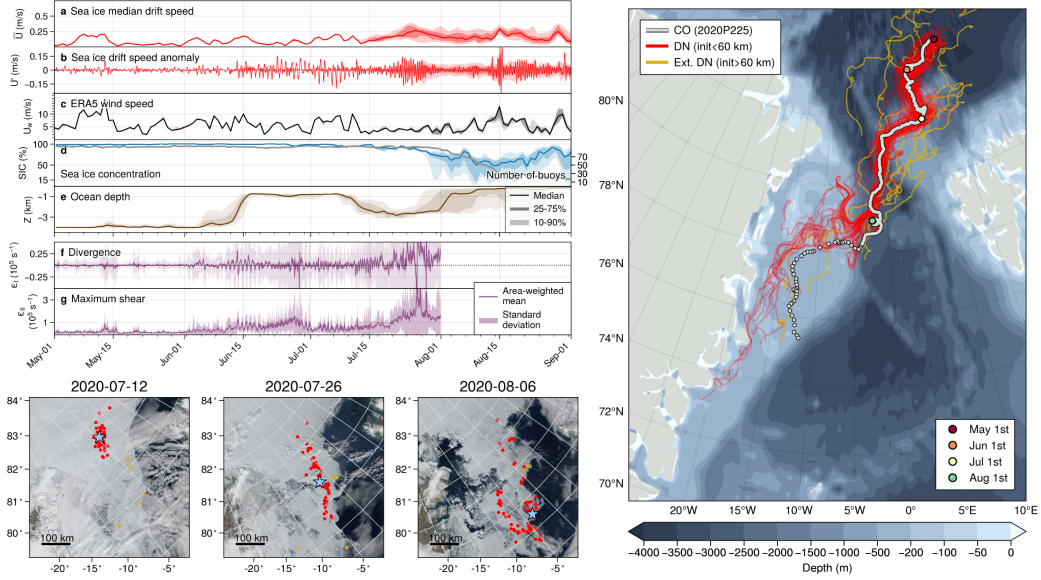


Figure 1. Top left: (a-e) Ensemble distribution of daily medians of observations and conditions for the Distributed Network. Lines indicate ensemble median, while dark and light shading represents the interquartile range and interdecile range respectively. Time series from top to bottom are (a) daily median drift speed, (b) drift speed anomaly (residual after removing daily median speed), (c) ERA5 wind speed, (d) sea ice concentration, (e) ocean depth at buoy positions. Wind speed, depth, and sea ice concentration are interpolated to buoy positions. Observations with estimated sea ice concentration less than 15% were masked prior to calculating percentiles. Panels (f) and (g) show area-weighted means (solid lines) and standard deviations (shading) of divergence and maximum total shear strain rates. Lower left: Buoy positions and sea ice conditions on July 12th (h), July 26th (i), and August 6th (j). The blue star marks the location of 2020P225, which was located at the Central Observatory. Imagery from MODIS accessed through NASA WorldView. Right: Drift trajectories for buoys within the Distributed Network (red) and additional buoys (gold) overlaid on ocean bathymetry. The light gray trajectory corresponds to buoy 2020P225 as in panels (h-j). The dotted portion of the trajectory marks locations where interpolation with the satellite product indicates 0% SIC and MODIS imagery shows that the buoy is next to the ice edge. Colored circles mark the first day of each month.

160 During the initial stage, the array remained in pack ice over the Nansen Basin (May
 161 1st to June 13th, Figure 1). Drift speeds were low (median speed 7 cm/s) except for the
 162 second week of May, coinciding with a strong cyclone. This event induced deformation
 163 in the array that peaked at the time of maximum wind speed. As the array drifted over
 164 the Yermak Plateau (June 13-July 12), drift speed increases up to 14 cm/s. Deforma-
 165 tion rates began to increase as the first few buoys moved into a shallower region. The
 166 ensemble median drift speed anomaly increased as the array drifted over the plateau bound-
 167 ary displaying an apparent diurnal oscillation. Note that the wind speed was not notice-
 168 ably different from that of the previous month, suggesting the importance of ocean forc-
 169 ing. Both divergence and shear increased at this time. Divergence, like the sub-daily ve-
 170 locity, showed a diurnal oscillation pattern. The oscillation is evidence of working leads
 171 repeatedly opening and closing. A similar feature was noted during the N-ICE2015 cam-
 172 paign, suggesting that this diurnal pattern is a recurring feature of the region (Itkin et
 173 al., 2017). Earlier measurements of divergence in ocean currents suggest tides as a mech-
 174 anism for this feature (Padman et al., 1992). This possibility will be examined in Sec-
 175 tion 5. The periodic changes in divergence preceded the oscillation in the median drift
 176 speed anomaly, hinting at the role of internal ice stresses inducing deformation.

177 From July 12-August 1 the buoy array drifted southward within the East Green-
 178 land Channel and experienced widespread positive divergence and increasing shear, stretch-
 179 ing the array on roughly a north-south axis (Figure 1 in panel h and i). Prior to this point,
 180 the structure of the deployment array had not undergone significant changes. Sea ice con-
 181 centration decreased markedly, and we see an increase in 12-hourly oscillations relative
 182 to the daily median. Wind speeds were lowest during this period, indicating that the in-
 183 crease in drift speeds must have come from either decreased ice stresses or increased ocean
 184 forcing. The role of wind forcing will be explored in Section 4.

185 Deteriorating ice conditions (Figure 1, panel j) led to the decision at the end of July
 186 to dismantle the CO and retrieve many of the autonomous sensors (Nicolaus et al., 2022).
 187 By August 1st the main floe had broken apart. A portion of the remaining array drifted
 188 southeast and appeared to be drawn into a large eddy, while the rest of the array drifted
 189 southwest onto East Greenland Shelf (Figure 1 panels j, k). The late summer ice pack
 190 comprised distinct floes among patches of open water. The proximity of filaments of sea
 191 ice drawn into vortices indicates the presents of mesoscale ocean eddies. A mid-August
 192 storm lead to a spike in drift speeds and was followed by enhanced sub-daily, oscillatory
 193 variability. By the end of August, all but 12 buoys had drifted into ice-free waters or ceased
 194 operation.

195 4 Relationship between wind and ice velocity at daily timescales

196 The majority of daily to monthly sea ice drift variability in the central Arctic can
 197 be explained by variability in the wind (e.g., Thorndike and Colony (1982)). Thus mo-
 198 tivated, we begin by assuming a simple relationship between ice and wind

$$U = \alpha e^{-i\theta} U_a + \epsilon \quad (2)$$

199 where $U = u+iv$ is the complex drift speed, α is a transfer coefficient, which we
 200 refer to as the drift speed ratio, θ is the turning angle, $U_a = u_a + iv_a$ is the complex
 201 wind speed, and ϵ is the residual. The residual ϵ includes effects of ocean currents, sea
 202 surface slope, inertia, Coriolis force, and internal ice stresses, as well as error in the choice
 203 of α and θ and error in the ERA5 wind field. Oceanic, atmospheric, and internal ice stresses
 204 are an order of magnitude larger than the remaining terms, so we focus on these (Leppäranta,
 205 2007). Changes in ϵ thus provide an indicator of changes in the key forcings for ice mo-
 206 tion. The median drift speed ratio over the study period is $\alpha = 0.021$ and the median
 207 turning angle is 20° , in line with previous Arctic Ocean-wide estimates (Brunette et al.,

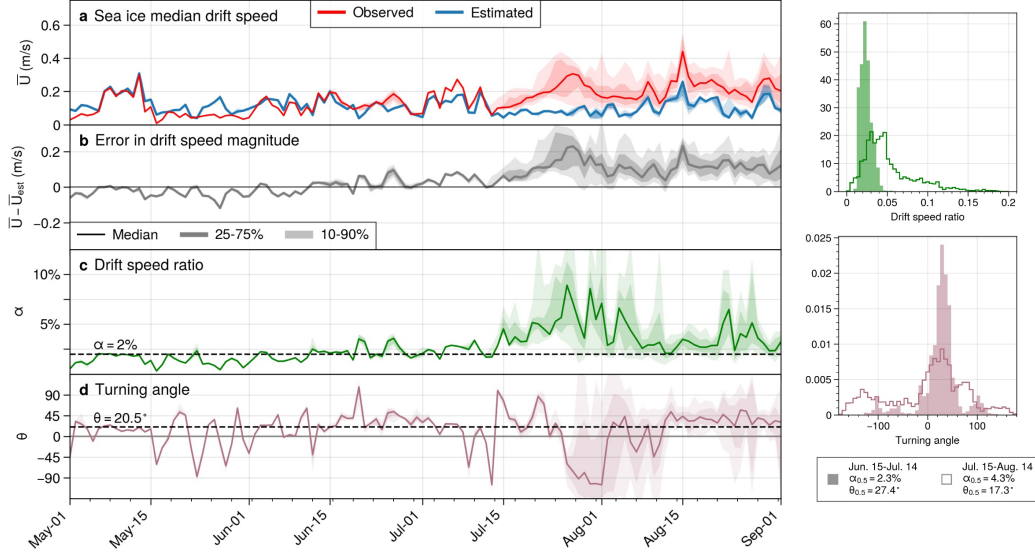


Figure 2. Left: (a) Observed daily median drift speed (red) compared to estimated drift speed (blue), (b) residual of drift speed magnitude, (c) drift speed ratio, (d) turning angle. Solid lines show the ensemble median, and dark and light shading shows the 25-75% and 10-90% ranges. Dashed lines in (b) and (c) mark the May-August median values of the drift speed ratio and turning angles. Right: Histogram estimates of probability density functions for drift speed ratio (e) and turning angle (f). Shaded and outlined distributions summarize the 30 day periods prior to and following July 15th, respectively.

208 2022, e.g.). Applying these values to Eq. 2 results in the estimated wind speed $U_{est} =$
 209 $\alpha e^{-i\theta} U_a$ depicted in Figure 2, panel a.

210 The wind model tends to overestimate the drift speed slightly from May to early
 211 June consistent with ice stresses acting against the wind stress. Thereafter, the error in
 212 drift speed magnitude $\epsilon_s = |U| - |U_{est}|$ grows, as does variability in U . The closest agree-
 213 ment to the theoretical value comes when wind speeds are high, (e.g. during the storm
 214 in early May), suggesting that the ice approaches free drift during these events. Sustained
 215 low wind speeds in mid-to-late July coincided with increased magnitude of ϵ_s . Follow-
 216 ing July 15th, α becomes strongly right-skewed and the median value increases; mean-
 217 while, median θ is close to the same but the likelihood of large deviations increases. Given
 218 the low sea ice concentration in the region (Figure 1 panels i, j), it is unlikely that the
 219 deviations are due to increases in ice stress. Rather, we surmise that ocean forcing is play-
 220 ing a larger role in ice dynamics at daily timescales from mid-July onward.

221 The number of buoys decreases as the drift proceeds onto the Greenland Shelf. To
 222 supplement the investigation of ice drift variability in the shelf region we turn to the Ice
 223 Floe Tracker (IFT). The majority of IFT observations are from the East Greenland Shelf
 224 between 70 and 80 N (Figure 3 panel a). Low drift speeds along the coast are the result
 225 of frequently occurring landfast ice. Drift speeds are enhanced along the shelf bound-
 226 ary (Figure 3 panel b). While a small gradient in wind speed contributes to the drift speed
 227 gradient, the residuals from the drift model are nearly the same magnitude as the over-
 228 all drift speed, indicating a major role for ocean currents. For most of the region, this
 229 area of enhanced drift speed is also the ice edge. Further north, in the East Greenland
 230 Channel, we find local maxima in drift speed away from the ice edge along the shelf bound-

231 ary. Drift direction, too, tends to follow the shelf boundary. On the northwest corner
 232 of the shelf, we see some evidence of a re-circulation pattern with northward flow along
 233 the coast turning clockwise to join the southward flow, consistent with model results from
 234 (Richter et al., 2018).

235 Empirical estimates of the distribution of turning angles and drift speed ratios for
 236 the 20 years of summer IFT data (Figure 3) indicate that both quantities are highly vari-
 237 able and depend on the wind speed. The turning angle distribution for the IFT data is
 238 bimodal. Peaks in the θ distribution correspond to the expected 20 degree turning an-
 239 gle and to the reverse of the wind direction. The ice nearly always moves southward along
 240 the coast, and the wind is mainly aligned along shore, favoring the southwest direction.
 241 Under southerly winds, the ice as a whole does not tend to change directions. In most
 242 cases, when the turning angle is close to -180° , the wind direction is southerly (not shown).
 243 The highest variability in turning angles and drift speed ratios is at low wind speeds. As
 244 the wind speeds increase they come to dominate control of ice drift over the ocean cur-
 245 rents.

246 For comparison with IFT, we downsample the buoy drift trajectories to 00:00 UTC,
 247 the approximate time of the MODIS daytime overpass, and re-calculate velocity from
 248 daily displacements. Empirical distributions of θ and α for the period from July 15th
 249 onward are shown in Figure 3. This period is when the majority of the MOSAiC array
 250 is within the region sampled by IFT. Due to the relatively small sample size, the buoy-
 251 derived distribution is less evenly sampled than the IFT distribution, yet we see that the
 252 main features are reproduced. At wind speeds lower than 7.5 m/s, we are much more
 253 likely to see high variability in both the turning angle and in the drift speed ratio. Drift
 254 speed ratios at high wind speeds are higher in the buoy data than in IFT, which may
 255 be due to differences in spatial sampling. As seen in Figure 3, panel b, the highest me-
 256 dian drift speeds are found along the shelf break and within the East Greenland Chan-
 257 nel, where many of the buoys were located.

258 5 Sub-daily sea ice variability, inertial oscillations, and tides

259 We now quantify the apparent tide-like oscillation seen in Figure 1. We select 20-
 260 day segments of buoy trajectories from four distinct bathymetric regions: the Nansen
 261 Basin (NB), the Yermak Plateau (YP), East Greenland Channel (GC), and East Green-
 262 land Shelf (GS) (Figure 4a). Rotary spectra show distinct characteristics, with strong
 263 signals in both semi-diurnal and diurnal frequency bands everywhere except the deep
 264 Nansen Basin (Figure 4, b-e) indicating that tidal currents play an important role in sub-
 265 daily sea ice velocity variability. In the northern hemisphere, inertial oscillations are clock-
 266 wise (CW), which manifests as higher spectral power in the CW direction than in the
 267 counterclockwise (CCW). The peak in the semidiurnal band for the Nansen Basin tra-
 268 jectories is small but exists in both CW and CCW components. This suggests the pos-
 269 sibility of tidal effects on ice motion even in pack ice well away from the shelves. We note
 270 as a topic for future research that the the east-west velocity component displays a reg-
 271 ular semi-diurnal oscillation that is not apparent in the north-south velocity component.

272 The spread of spectral power across the array (indicated by the shading and dot-
 273 ted lines in Figure 4) is smaller in the NB and YP than in the channel and shelf, reflect-
 274 ing both the coherence expected in pack ice and the area sampled. The CCW semi-diurnal
 275 peak is narrow and strong in the GC suggesting a clearer influence of semi-diurnal tides.
 276 Over the GS, the diurnal band is no longer distinct, while the semi-diurnal CW band
 277 remains strong but increases in spread. Since the shelf region includes a wider range of
 278 buoy locations, it is possible that interacting tidal waves and varied bottom topography
 279 dilute the tidal signal. Sensor failure and sensor retrieval results in a smaller sample size
 280 (26 buoys) representing a region nearly twice as large as the region sampled over the YP,
 281 further contributing to the spread in the spectral peak.

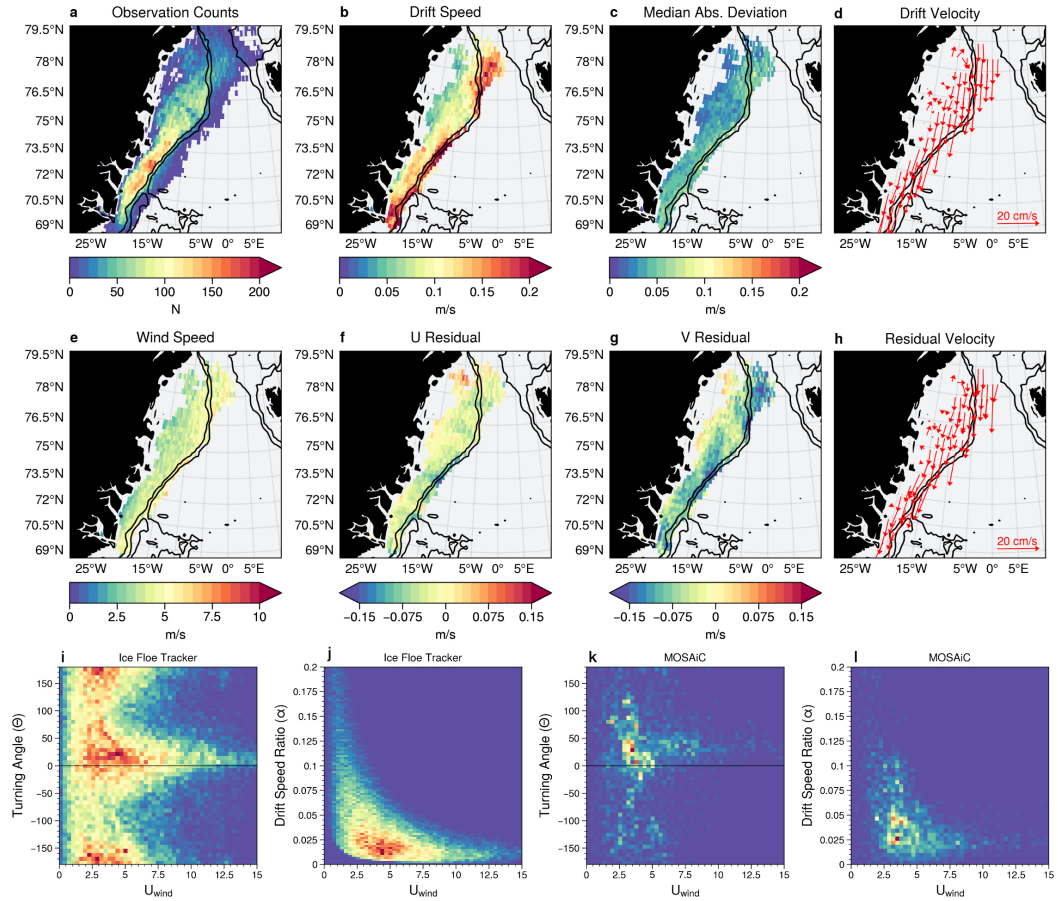


Figure 3. Top and middle rows: IFT results binned to a 0.25° latitude by 0.5° longitude grid. Velocities are binned by taking the median within grid cells. (a) Number of observations (b) Median drift speed within each grid cell (c) Median absolute deviation of drift speed (d) Drift velocity (every 3rd grid cell plotted) (e) ERA5 wind speed interpolated to floe locations (f) u component of residual (g) v component of residual (h) residual velocity. Residuals in (f,g,h) relative to wind-driven free drift model. Bottom row: empirical estimates of the joint distributions of ERA5 wind speed and (e) IFT observations of turning angles (f) IFT observations of drift speed ratios (g) MOSAiC observations of turning angles (h) MOSAiC observations of drift speed ratios.

282 The harmonic model assumes that hourly velocity anomalies occur at a limited set
 283 of tidal frequencies. When the harmonic model performs well, we interpret that the sub-
 284 daily sea ice velocity is consistent with tidal forcing. Tidal constituents are typically es-
 285 timated from measurements of ocean currents or sea surface height, not sea ice motion;
 286 we expect that the additional variability due to imperfect momentum transfer between
 287 the surface current and the motion of the ice pack will make the estimate of tidal vari-
 288 ability more uncertain. It is therefore notable that we find such strong tidal signals in
 289 the ice motion. Implied maximum currents of between 0.1 m/s and 0.2 m/s are seen over
 290 the shelf, channel, and plateau, consistent with other tidal current speed estimates (Padman
 291 & Erofeeva, 2004; Padman et al., 1992; Vasulkar et al., 2022). These speeds are close to
 292 the total drift velocity, hence, tidal currents are likely a major component of ice motion
 293 in these regions. For the Yermak Plateau, more than 80% of the sub-daily variance is
 294 explained by the tidal currents. The strong change in ocean forcing from the Nansen Basin
 295 onto the Yermak Plateau implies a sharp gradient in the ice velocity, inducing deformation.
 296 This is confirmed in Figure 1, where we see diurnal oscillation in both divergence
 297 and maximum shear that coincides with arrival of the MOSAiC array at the edge of Yer-
 298 mak Plateau.

299 Inertial oscillations are difficult to differentiate from semi-diurnal tidal variability
 300 at high latitudes. Not only are individual semi-diurnal tidal components very close to
 301 the inertial period, but tidally generated waves can become inertially trapped. Confi-
 302 dence that the semi-diurnal cycles can be attributed to tides comes from the relatively
 303 long 20-day time window used for estimating tidal constituents, and the presence of strong
 304 peaks in the CCW band of the rotary spectra. The presence of inertial oscillations in ad-
 305 dition to the tidal variability is indicated by the strong CW peaks in the rotary spec-
 306 tra as well as the timing of increases in sub-daily velocity anomalies following brief pe-
 307 riods of strong winds, such as occurred on August 15th.

308 6 Discussion and conclusion

309 The MOSAiC ice drift observations capture a broad range of summer ice dynam-
 310 ics in a historically undersampled region. The spatial coverage in our study allows us to
 311 document the imprint of differences in ocean forcing on sea ice dynamics across distinct
 312 bathymetric regions with unprecedented fidelity. Ice drift has a strong stochastic com-
 313 ponent due to the interaction of highly variable wind and ocean forcing. The particu-
 314 lar path taken by the MOSAiC observatory resulted in a month-long residence over the
 315 tidally active Yermak Plateau. Gradients in velocity due to the abrupt transition between
 316 the basin and tidally active plateau impose strain on the ice, enhancing deformation. Sub-
 317 sequent low wind speeds, decreasing ice concentration, and the proximity of boundary
 318 currents resulted in ocean currents dominating the drift through the Fram Strait. Fol-
 319 lowing transit through the Fram Strait, intermittent high drift speed events result from
 320 strong wind events, and both tides and inertial oscillations affect the subdaily drift ve-
 321 locities. Low ice concentration late in the summer resulted in the MOSAiC observatory
 322 being more sensitive to changes in atmosphere and ocean forcing, unconstrained by in-
 323 ternal ice stresses.

324 Our results emphasize the importance of small-scale, sub-daily motion for ice dy-
 325 namics (Heil et al., 2008; Itkin et al., 2017). We show that a substantial fraction of ob-
 326 served sea ice velocity at hourly timescales occurs at tidal and inertial frequencies. Char-
 327 acteristics of this variability are distinct within regions defined by bathymetry. Uncer-
 328 tainty in bathymetry combined with sparsely located tide gauges means that tides are
 329 poorly constrained throughout the shallow Arctic marginal seas. Models of sea ice drift
 330 that fail to take mesoscale ocean variability and tides into account will systematically
 331 underestimate drift variability and deformation. The range of dynamical regimes cap-
 332 tured during the MOSAiC drift provides a challenging test case for next-generation, tide-
 333 resolving coupled sea ice models.

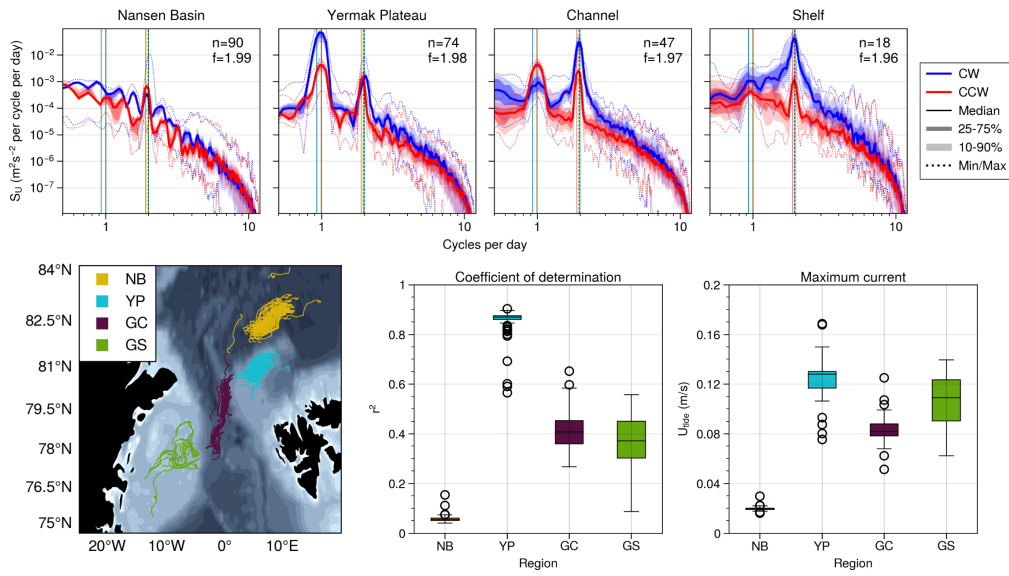


Figure 4. Top: Periodograms of rotary spectra for (a) the Nansen Basin (NB), (b) Yermak Plateau (YP), (c) East Greenland Channel (GC), and the (d) East Greenland Shelf (GS). Dotted lines show the minimum and maximum across the n trajectories. Shading and solid lines show percentile estimates of distributions and the median, respectively. Blue indicates clockwise rotation and red indicates counterclockwise rotation. Bottom, from left to right: (e) Trajectory segments used for frequency analysis (colored by region), (f) box-and-whisker plot of the coefficient of determination (percent variance explained) and (g) box-and-whisker plot of the daily maximum tidal current.

334 Motion at daily timescales in the Fram Strait summer marginal ice zone bears a
 335 spatially heterogeneous imprint of ocean forcing. As ice concentration decreases and ice
 336 moves closer to the ice edge, the drift speed ratio increases, and the ice drift becomes
 337 less spatially coherent. The wide range of observed turning angles and drift speeds in-
 338 dicate an important role for ocean variability. As we showed through the IFT drift statis-
 339 tics, such variability is not limited to the MOSAiC observational period for the Green-
 340 land Shelf region, but is a typical feature of this highly dynamic region.

341 7 Open Research

342 MOSAiC drift tracks are freely available from the Arctic Data Center (Bliss et al.,
 343 2022). 10m wind data from ERA5 is available at the Copernicus Data Store (Hersbach
 344 et al., 2018). IBCAO bathymetric data at 400 m by 400 m resolution was downloaded
 345 from https://www.gebco.net/data_and_products/gridded_bathymetry_data/arctic_ocean/. Ice Floe Tracker trajectories, derived data and code used for this analysis are
 346 available at <https://doi.org/10.5281/zenodo.7996638>.

348 We acknowledge the use of MODIS True Color Corrected Reflectance imagery from
 349 the Terra and Aqua satellites acquired via the from the Worldview Snapshots application
 350 (<https://wvs.earthdata.nasa.gov>), part of the Earth Observing System Data and Infor-
 351 mation System (EOSDIS).

352 Analysis was carried out using the open source Python scientific computing stack,
 353 and we wish to acknowledge the contributions of volunteer developers who maintain and
 354 develop this resource. Data analysis was performed using xarray (Hoyer & Hamman, 2017),
 355 pandas (pandas development team, 2020), NumPy (Harris et al., 2020), and SciPy (Virtanen
 356 et al., 2020). Figures were prepared using the ProPlot Python library (Davis, 2021).

357 Acknowledgments

358 DW, JH, and MMW were supported by NASA The Science of Terra, Aqua, and Suomi-
 359 NPP Program (20-TASNPP20-0202). DW and JH were also supported by the Depart-
 360 ment of Energy Atmospheric Systems Research (13016524). AB, DW, and JH were also
 361 supported by the National Science Foundation (1722729). AB was also supported by NASA's
 362 Internal Scientist Funding Model in the Cryospheric Sciences Laboratory. MMW was
 363 also supported by the Office of Naval Research (ONR) Arctic Program (N00014-20-1-
 364 2753, N00014-22-1-2741, and N00014-22-1-2722) and the ONR Multidisciplinary Uni-
 365 versity Research Initiatives Program (N00014-23-1-2014).

366 Drift track data used in this manuscript was produced as part of the international
 367 Multidisciplinary drifting Observatory for the Study of the Arctic Climate (MOSAiC)
 368 with the tag MOSAiC20192020 and the Project_ID: AWLPS122_00. The authors acknowl-
 369 edge the data collection and processing efforts of the MOSAiC science and logistics teams
 370 and of all those who contributed to MOSAiC and made this endeavour possible (Nix-
 371 dorf et al. 2021).

372 The authors declare no conflicts of interest.

373 References

- 374 Arbic, B. K. (2022, August). Incorporating tides and internal gravity waves within
 375 global ocean general circulation models: A review. *Progress in Oceanography*,
 376 *206*, 102824. doi: 10.1016/j.pocean.2022.102824
- 377 Bliss, A. C., Hutchings, J. K., Anderson, P., Anhaus, P., & Belter, H. J. (2022).
 378 *Sea ice drift tracks from the Distributed Network of autonomous buoys de-*
 379 *ployed during the Multidisciplinary drifting Observatory for the Study of*

- 380 *Arctic Climate (MOSAiC) expedition 2019-2021*. Arctic Data Center. doi:
381 doi:10.18739/A2KP7TS83
- 382 Boylan, B. M. (2021, September). Increased maritime traffic in the Arctic: Implica-
383 tions for governance of Arctic sea routes. *Marine Policy*, *131*, 104566. doi: 10
384 .1016/j.marpol.2021.104566
- 385 Brunette, C., Tremblay, L. B., & Newton, R. (2022). A new state-dependent param-
386 eterization for the free drift of sea ice. *Cryosphere*, *16*(2), 533–557. doi: 10
387 .5194/tc-16-533-2022
- 388 Comiso, J. C., Meier, W. N., & Gersten, R. (2017). Variability and trends in the
389 Arctic Sea ice cover: Results from different techniques. *Journal of Geophysical*
390 *Research: Oceans*, *122*(8), 6883–6900. doi: 10.1002/2017JC012768
- 391 Davis, L. L. B. (2021, October). *Proplot*. Zenodo. Retrieved from [https://doi](https://doi.org/10.5281/zenodo.5602155)
392 [.org/10.5281/zenodo.5602155](https://doi.org/10.5281/zenodo.5602155) doi: 10.5281/zenodo.5602155
- 393 Dawson, J., Pizzolato, L., Howell, S. E., Copland, L., & Johnston, M. E. (2018,
394 February). Temporal and Spatial Patterns of Ship Traffic in the Canadian Arctic
395 from 1990 to 2015 + Supplementary Appendix 1: Figs. S1–S7 (See Article
396 Tools). *ARCTIC*, *71*(1). doi: 10.14430/arctic4698
- 397 Dumont, D. (2022, October). Marginal ice zone dynamics: History, definitions
398 and research perspectives. *Philosophical Transactions of the Royal Society A:*
399 *Mathematical, Physical and Engineering Sciences*, *380*(2235), 20210253. doi:
400 10.1098/rsta.2021.0253
- 401 Feldl, N., Po-Chedley, S., Singh, H. K., Hay, S., & Kushner, P. J. (2020). Sea
402 ice and atmospheric circulation shape the high-latitude lapse rate feed-
403 back. *npj Climate and Atmospheric Science*, *3*(1), 1–9. doi: 10.1038/
404 s41612-020-00146-7
- 405 Fer, I., Müller, M., & Peterson, A. K. (2015, March). Tidal forcing, energetics, and
406 mixing near the Yermak Plateau. *Ocean Science*, *11*(2), 287–304. doi: 10
407 .5194/os-11-287-2015
- 408 Foldvik, A., Aagaard, K., & Tørresen, T. (1988, August). On the velocity field
409 of the East Greenland Current. *Deep Sea Research Part A. Oceanographic Re-*
410 *search Papers*, *35*(8), 1335–1354. doi: 10.1016/0198-0149(88)90086-6
- 411 Gimbert, F., Marsan, D., Weiss, J., Jourdain, N. C., & Barnier, B. (2012). Sea ice
412 inertial oscillations in the Arctic Basin. *Cryosphere*, *6*(5), 1187–1201. doi: 10
413 .5194/tc-6-1187-2012
- 414 Harris, C. R., Millman, K. J., van der Walt, S. J., Gommers, R., Virtanen, P., Cour-
415 napeau, D., ... Oliphant, T. E. (2020, September). Array programming with
416 NumPy. *Nature*, *585*(7825), 357–362. Retrieved from [https://doi.org/](https://doi.org/10.1038/s41586-020-2649-2)
417 [10.1038/s41586-020-2649-2](https://doi.org/10.1038/s41586-020-2649-2) doi: 10.1038/s41586-020-2649-2
- 418 Hatcher, S., Ahmed, A., Kim, M., & Wilhelmus, M. M. (2022, April). *SOIT: Satel-*
419 *lite overpass identification tool*. Zenodo. Retrieved from [https://doi.org/10](https://doi.org/10.5281/zenodo.6475619)
420 [.5281/zenodo.6475619](https://doi.org/10.5281/zenodo.6475619) doi: 10.5281/zenodo.6475619
- 421 Heil, P., Hutchings, J. K., Worby, A. P., Johansson, M., Launiainen, J., Haas, C.,
422 & Hibler, W. D. (2008, April). Tidal forcing on sea-ice drift and deformation
423 in the western Weddell Sea in early austral summer, 2004. *Deep Sea*
424 *Research Part II: Topical Studies in Oceanography*, *55*(8-9), 943–962. doi:
425 10.1016/j.dsr2.2007.12.026
- 426 Hersbach, H., Bell, B., Berrisford, P., Biavati, G., Horányi, A., Muñoz Sabater, J.,
427 ... Thépaut, J.-n. (2018). *ERA5 hourly data on single levels from 1959 to*
428 *present*. Copernicus Climate Change Service (C3S) Climate Data Store (CDS).
429 doi: 10.24381/cds.adbb2d47
- 430 Hersbach, H., Bell, B., Berrisford, P., Hirahara, S., Horányi, A., Nicolas, J., ...
431 Thépaut, J.-n. (2020). The ERA5 global reanalysis. *Quarterly Journal of the*
432 *Royal Meteorological Society*, 1999–2049. doi: 10.1002/qj.3803
- 433 Hoyer, S., & Hamman, J. (2017, April). Xarray: N-D labeled Arrays and Datasets in
434 Python. *Journal of Open Research Software*, *5*(1), 10. doi: 10.5334/jors.148

- 435 Hutchings, J. K., Heil, P., Steer, A., & Hibler, W. D. (2012). Subsynoptic scale
 436 spatial variability of sea ice deformation in the western Weddell Sea during
 437 early summer. *Journal of Geophysical Research*, *117*(C1), C01002. doi:
 438 10.1029/2011JC006961
- 439 Hutchings, J. K., Roberts, A., Geiger, C. A., & Richter-Menge, J. (2011). Spa-
 440 tial and temporal characterization of sea-ice deformation. *Annals of Glaciol-
 441 ogy*, *52*(57 PART 2), 360–368. doi: 10.3189/172756411795931769
- 442 Hutchings, J. K., Roberts, A., Geiger, C. A., & Richter-Menge, J. (2018). Corrigen-
 443 dum: Spatial and temporal characterisation of sea-ice deformation. *Journal of
 444 Glaciology*, *64*(244), 343–346. doi: 10.1017/jog.2018.11
- 445 Itkin, P., Spreen, G., Cheng, B., Doble, M., Girard-Ardhuin, F., Haapala, J.,
 446 ... Wilkinson, J. (2017, June). Thin ice and storms: Sea ice defor-
 447 mation from buoy arrays deployed during N-ICE2015: THIN ICE AND
 448 STORMS. *Journal of Geophysical Research: Oceans*, *122*(6), 4661–4674.
 449 doi: 10.1002/2016JC012403
- 450 Jakobsson, M., Mayer, L. A., Bringenspar, C., Castro, C. F., Mohammad, R., John-
 451 son, P., ... Zinglensen, K. B. (2020). The International Bathymetric Chart of
 452 the Arctic Ocean Version 4.0. *Scientific Data*, *7*(176), 14.
- 453 Kozlov, I. E., Plotnikov, E. V., & Manucharyan, G. E. (2020, September). Brief
 454 Communication: Mesoscale and submesoscale dynamics in the marginal ice
 455 zone from sequential synthetic aperture radar observations. *The Cryosphere*,
 456 *14*(9), 2941–2947. doi: 10.5194/tc-14-2941-2020
- 457 Krumpfen, T., & Sokolov, V. (2020). *The Expedition AF122/1 Setting up the MO-
 458 SAiC Distributed Network in October 2019 with Research Vessel Akademik
 459 Fedorov* (Tech. Rep. No. October 2019). Potsdam, Germany: Alfred Wegener
 460 Institute.
- 461 Kwok, R. (2010). Satellite remote sensing of sea-ice thickness and kinemat-
 462 ics: A review. *Journal of Glaciology*, *56*(200), 1129–1140. doi: 10.3189/
 463 002214311796406167
- 464 Lammert, A., Brümmer, B., & Kaleschke, L. (2009, May). Observation of cyclone-
 465 induced inertial sea-ice oscillation in Fram Strait. *Geophysical Research Let-
 466 ters*, *36*(10), L10503. doi: 10.1029/2009GL037197
- 467 Leppäranta, M. (2007). *The drift of sea ice*. Springer Berlin Heidelberg. Retrieved
 468 from <https://books.google.com/books?id=MMIXa011jxwC>
- 469 Leppäranta, M., & Hibler, W. D. (1987). Mesoscale sea ice deformation in the East
 470 Greenland marginal ice zone. *Journal of Geophysical Research*, *92*(C7), 7060.
 471 doi: 10.1029/JC092iC07p07060
- 472 Lopez-Acosta, R., Schodlok, M. P., & Wilhelmus, M. M. (2019). Ice Floe Tracker:
 473 An algorithm to automatically retrieve Lagrangian trajectories via feature
 474 matching from moderate-resolution visual imagery. *Remote Sensing of Envi-
 475 ronment*, *234*(October), 111406. doi: 10.1016/j.rse.2019.111406
- 476 Manucharyan, G. E., Lopez-Acosta, R., & Wilhelmus, M. M. (2022). Spinning ice
 477 floes reveal intensification of mesoscale eddies in the western Arctic Ocean.
 478 *Scientific Reports*, *12*(7070).
- 479 Maslanik, J. A., Fowler, C., Stroeve, J., Drobot, S., Zwally, J., Yi, D., & Emery,
 480 W. (2007). A younger, thinner Arctic ice cover: Increased potential for rapid,
 481 extensive sea-ice loss. *Geophysical Research Letters*, *34*(24), 2004–2008. doi:
 482 10.1029/2007GL032043
- 483 Meier, W. N., T. M., & Comiso, J. C. (2018). *AMSR-E/AMSR2 unified L3 daily
 484 12.5 km brightness temperatures, sea ice concentration, motion & snow depth
 485 polar grids, version 1*. NASA National Snow and Ice Data Center Distributed
 486 Active Archive Center. doi: 10.5067/RA1MLJOYPK3P
- 487 Morison, J. H., McPhee, M. G., & Maykut, G. A. (1987). Boundary layer, upper
 488 ocean, and ice observations in the Greenland Sea Marginal Ice Zone. *Journal
 489 of Geophysical Research*, *92*(C7), 6987. doi: 10.1029/JC092iC07p06987

- 490 Nicolaus, M., Perovich, D. K., Spreen, G., Granskog, M. A., von Albedyll, L., An-
 491 gelopoulos, M., . . . Wendisch, M. (2022, 02). Overview of the MOSAiC
 492 expedition: Snow and sea ice. *Elementa: Science of the Anthropocene*, *10*(1).
 493 Retrieved from <https://doi.org/10.1525/elementa.2021.000046> (000046)
 494 doi: 10.1525/elementa.2021.000046
- 495 Padman, L., & Erofeeva, S. (2004, January). A barotropic inverse tidal
 496 model for the Arctic Ocean. *Geophysical Research Letters*, *31*(2). doi:
 497 10.1029/2003GL019003
- 498 Padman, L., Plueddemann, A. J., Muench, R. D., & Pinkel, R. (1992). Diurnal tides
 499 near the Yermak Plateau. *Journal of Geophysical Research*, *97*(C8), 12639.
 500 doi: 10.1029/92JC01097
- 501 pandas development team, T. (2020, February). *Pandas-dev/pandas: Pandas*. Zen-
 502 odo. doi: 10.5281/zenodo.3509134
- 503 Pease, C. H., Turet, P., & Pritchard, R. S. (1995). Barents Sea tidal and inertial mo-
 504 tions from Argos ice buoys during the Coordinated Eastern Arctic Experiment.
 505 *Journal of Geophysical Research*, *100*(C12), 24705. doi: 10.1029/95JC03014
- 506 Polyakov, I. V., Rippeth, T. P., Fer, I., Baumann, T. M., Carmack, E. C., Ivanov,
 507 V. V., . . . Rember, R. (2020, August). Intensification of Near-Surface Currents
 508 and Shear in the Eastern Arctic Ocean. *Geophysical Research Letters*, *47*(16).
 509 doi: 10.1029/2020GL089469
- 510 Quadfasel, D., Gascard, J.-C., & Koltermann, K.-P. (1987). Large-scale oceanogra-
 511 phy in Fram Strait during the 1984 Marginal Ice Zone Experiment. *Journal of*
 512 *Geophysical Research*, *92*(C7), 6719. doi: 10.1029/JC092iC07p06719
- 513 Richter, M. E., von Appen, W.-J., & Wekerle, C. (2018, September). Does the East
 514 Greenland Current exist in the northern Fram Strait? *Ocean Science*, *14*(5),
 515 1147–1165. doi: 10.5194/os-14-1147-2018
- 516 Smedsrud, L. H., Halvorsen, M. H., Stroeve, J. C., Zhang, R., & Kloster, K. (2017,
 517 January). Fram Strait sea ice export variability and September Arctic sea ice
 518 extent over the last 80 years. *The Cryosphere*, *11*(1), 65–79. doi: 10.5194/tc-11-
 519 -65-2017
- 520 Squire, V. A. (2020, January). Ocean Wave Interactions with Sea Ice: A
 521 Reappraisal. *Annual Review of Fluid Mechanics*, *52*(1), 37–60. doi:
 522 10.1146/annurev-fluid-010719-060301
- 523 Stammer, D., Ray, R. D., Andersen, O. B., Arbic, B. K., Bosch, W., Carrère, L., . . .
 524 Yi, Y. (2014, September). Accuracy assessment of global barotropic ocean tide
 525 models. *Reviews of Geophysics*, *52*(3), 243–282. doi: 10.1002/2014RG000450
- 526 Taylor, P. C., Boeke, R. C., Boisvert, L. N., Feldl, N., Henry, M., Huang, Y., . . .
 527 Tan, I. (2022, February). Process Drivers, Inter-Model Spread, and the Path
 528 Forward: A Review of Amplified Arctic Warming. *Frontiers in Earth Science*,
 529 *9*, 758361. doi: 10.3389/feart.2021.758361
- 530 Thorndike, A., & Colony, R. (1982). Sea ice motion in response to geostrophic
 531 winds. *Journal of Geophysical Research*, *87*(C8), 5845–5852.
- 532 Tschudi, M. A., Meier, W. N., & Stewart, J. S. (2020, May). An enhancement to
 533 sea ice motion and age products at the National Snow and Ice Data Center
 534 (NSIDC). *The Cryosphere*, *14*(5), 1519–1536. doi: 10.5194/tc-14-1519-2020
- 535 Vasulkar, A., Verlaan, M., Slobbe, C., & Kaleschke, L. (2022, August). Tidal
 536 dissipation from free drift sea ice in the Barents Sea assessed using GNSS
 537 beacon observations. *Ocean Dynamics*, *72*(8), 577–597. doi: 10.1007/
 538 s10236-022-01516-w
- 539 Virtanen, P., Gommers, R., Oliphant, T. E., Haberland, M., Reddy, T., Courn-
 540 peau, D., . . . SciPy 1.0 Contributors (2020). SciPy 1.0: Fundamental algo-
 541 rithms for scientific computing in python. *Nature Methods*, *17*, 261–272. doi:
 542 10.1038/s41592-019-0686-2
- 543 Yoshizawa, E., Kamoshida, T., & Shimada, K. (2023, January). Sea Ice Motion
 544 Vector Retrievals from AMSR2 89-GHz Data: Validation Algorithm with Si-

545 multaneous Multichannel Observations. *Journal of Atmospheric and Oceanic*
546 *Technology*, 40(1), 3–13. doi: 10.1175/JTECH-D-22-0049.1
547 Zaron, E. D., & Elipot, S. (2021, January). An Assessment of Global Ocean
548 Barotropic Tide Models Using Geodetic Mission Altimetry and Surface
549 Drifters. *Journal of Physical Oceanography*, 51(1), 63–82. doi: 10.1175/
550 JPO-D-20-0089.1